

This is an *Accepted Manuscript*, which has been through the Royal Society of Chemistry peer review process and has been accepted for publication.

Accepted Manuscripts are published online shortly after acceptance, before technical editing, formatting and proof reading. Using this free service, authors can make their results available to the community, in citable form, before we publish the edited article. This Accepted Manuscript will be replaced by the edited, formatted and paginated article as soon as this is available.

You can find more information about *Accepted Manuscripts* in the **Information for Authors**.

Please note that technical editing may introduce minor changes to the text and/or graphics, which may alter content. The journal's standard <u>Terms & Conditions</u> and the <u>Ethical guidelines</u> still apply. In no event shall the Royal Society of Chemistry be held responsible for any errors or omissions in this *Accepted Manuscript* or any consequences arising from the use of any information it contains.





ARTICLE

Received 00th June 2016,

Structural discrimination of nanosilica particles and mixedstructure silica by multivariate analysis applied to SAXS profiles in combination with FT-IR spectroscopy

Accepted 00th July 2016

DOI: 10.1039/x0xx00000x

www.rsc.org/

Y. P. Ruiz, M. F. Ferrão, M. B. Cardoso, E. A. Moncada, and J. H. dos Santos E.

The structural characteristics of silica nanoparticles with functional properties can be investigated using Fourier transform infrared (FT-IR) and small-angle X-ray scattering (SAXS) techniques. Herein, principal component analysis (PCA) and hierarchical cluster analysis (HCA) were used to analyze the variance and to detect similarities between spectroscopic and scattering data. To analyze its potentiality, nanosilica and mixed-structure silica samples were synthesized by a sol-gel process using several reagents, such as SiCl₄, octadecylamine, Pluronic*L-31, and Tween*80, to modify the surfaces of silica nanoparticles. Additionally, the quantity of these reagents used in synthesis of the different particle types were studied in distinct levels. A total of 168 measurements (IR spectra and X-ray scatterings) were performed using 28 samples. The FT-IR/SAXS/multivariate analysis results suggest that samples can be separated into two major groups associated with the incorporation of organic groups into the silica network and the organizational structures of aggregates in the low-q region, which separated the surface fractals ($3.0 < P_L < 3.8$, class I) from the mass fractals ($1.7 < P_L < 2.8$, classes II and III). It was determined that only two principal components carried over 96.5 and 89.7 % of variance (FT-IR and SAXS, respectively) within the sample set. The organic groups in the hybrid mixed-structure silicas created more compact and denser silicas, increased the aggregate radii, decreased Dp_{BiH} and S_{BET}, and shifted the halo toward higher 20 angles due to the changes in the densities of the silicas. We demonstrate that the FT-IR and SAXS techniques combined with multivariate analysis can simplify the interpretation of changes in the structural properties of mesoporous silica materials.

1 Introduction

Spherical SiO_2 nanoparticles have been used in several areas, including electrochemistry, ¹ catalysis, ² coating, ³ chromatography ⁴ and controlled drug release. ⁵ The sol-gel process leads to the production of monodisperse SiO_2 microspheres with remarkable characteristics, such as large surface areas, small particle sizes, high mechanical and thermal stabilities, superior functional properties, controllable hydrophilicity or hydrophobicity, and low costs. ⁶

Currently, sol-gel materials have been synthesized by several methods, including the Stöber route using TEOS, ⁷ an acid-basic route using SiCl₄⁸ and an alternative route using surfactants. ⁹ Silica nanoparticles from the Stöber process have been used to fabricate rough surfaces and create superhydrophobic surfaces with micro- and nano-scale

To design silica particles with functional characteristics, structural analysis of this material is important because the interaction between the molecules (e.g., inorganic SiCl₄ or organic block copolymers) and the silica network surface is critical for the performance of this material. The structure can be investigated, for instance, by the Fourier transform infrared (FT-IR) and small-angle X-ray scattering (SAXS) methods. The FT-IR method can effectively provide a 'fingerprint' for the sample: characteristic spectral bands that can be used to determine parameters of the silica network,

structures simulating the self-cleaning function of a lotus leaf surface. The Starting from SiCl4, the attachment of Si-Cl groups onto a surface has been used to functionalize particles or modify their properties for chromatographic applications. Surfactants and block copolymers are widely used to control the template synthesis of mesoporous silica. These materials are effective in washing hydrophobic organic soils, e.g., removing tetrachloroethylene (PCE). Thus far, there are no studies that focus on the synthesis of nanosilicas on a micrometer silica surface, thus generating a mixed-structure silica, which combines the nanoscale and microscale properties. This approach could enhance the thermal stability of photocatalysts and may overcome a few of the size limitations due to the reuse of nanoscale photocatalysts. In the surface of the size limitations due to the reuse of nanoscale photocatalysts.

^{a.} Departamento de Engenharia Química - Universidade Federal do Rio Grande do Sul, Rua Engenheiro Luis Englert, CEP 90040-040, Porto Alegre, RS, Brazil.

b. Instituto de Química - Universidade Federal do Rio Grande do Sul, Av. Bento Gonçalves, CEP 91501-970, Porto Alegre, RS, Brazil.

^c LNLS – Laboratório Nacional de Luz Síncrotron, CEP 13083-970, Caixa Postal 6192, Campinas, SP, Brazil.

^d Instituto Tecnológico Metropolitano, Robledo, Calle 73 # 76 A 354, bloque F, Medellín, Colombia.

Electronic Supplementary Information (ESI) available: [details of any supplementary information available should be included here]. See DOI: 10.1039/x0xx00000x

ARTICLE RSC Advances

such as the function of the siloxane ring structure $((SiO)_6)$ with respect to the nanosilica porosity. ¹⁶ SAXS is a powerful and sensitive technique used to identify structural changes in materials when studying nanoparticles, thus allowing for the direct characterization of a system without requiring any pretreatment. Additionally, the SAXS offers structural information on size, polydispersity, and fractal structure. ^{17, 18} Due to its nature, the SAXS measurements reach the entire sample used in the experiment; thus, their results are statistically reliable because a large number of nanoparticles are probed during the experiment. ¹⁹

Recently, multivariate analyses have resulted in modeling the chemical and physical properties of simple and complex systems from spectroscopic data. 20,21,22 For instance, Veras et al.23 and Mueller et al.20 applied a principal component analysis (PCA) and hierarchical cluster analysis (HCA) to NIR spectroscopy for the unsupervised pattern recognition of biodiesel samples. Furthermore, FT-IR spectroscopy combined with multivariate data reduction has been used in the food industry, agriculture, and material characterization.^{24,25} PCA is sensitive to the presence of outliers and therefore to the presence of gross errors in datasets, which has led to several attempts to define robust variants of PCA.²⁶ Multivariate analysis has several specific advantages: it is rapid and simple, provides qualitative and quantitative results and can help reduce vast amounts of data to a scale where a relationship between the spectral features and the chemical composition can be formed. 27 However, there are no studies in the literature that combine the SAXS profiles with multivariate analysis. The association of the SAXS curves with other physicochemical characterization techniques via multivariate data analysis may provide a broader view of the entire system and a deeper understanding of the sample properties.

Hence, this is the first report correlating the structural characteristics (molecular and multi-organization hierarchical) of five types of silica nanoparticles and mixed-structure silica samples through simultaneous multivariate data analyses (PCA and HCA) applied using techniques with different principles, such as SAXS curves and FT-IR spectra. In this study, we monitored structural changes in different silica-based materials using several reagents, such as tetraethoxysilane, SiCl₄, octadecylamine, Pluronic®L-31, and Tween®80, as modifiers of the nanoparticle surfaces.

2 Experimental

2.1 Materials

The silica sols were prepared using tetraethoxysilane (TEOS, > 98%, Sigma-Aldrich) and ethanol (99.5%, Nuclear) as the solvent. An ammonium hydroxide solution (29%, Nuclear) was used as a catalyst. Silicon tetrachloride (SiCl₄, 99%, Sigma Aldrich) was used to chemically modify the silica sols. Octadecylamine (ODA, 97%), Pluronic®L-31 (Mn $^{\sim}$ 1100 Da, PEG, 10 wt. %), and Tween®80 (Mn $^{\sim}$ 1310 Da) were supplied by Sigma-Aldrich. Sylopol-948 (S_M, Grace) was used as the micrometric silica. All reagents were used as received.

2.2 Synthesis of standard, chemically modified, and hybrid nanosilicas

Five different methods were used to prepare the silica nanoparticles via the hydrolysis of TEOS using the sol-gel process described in the literature. The routes were labeled as follows: standard method (SG), chemical modification method with SiCl₄ (Cl), and hybrid method using ODA, Pluronic*L-31, and Tween*80 as the surfactant (Da, Pu and Tw, respectively). In the SG method, two solutions were prepared as follows: the first (A) was a mixture of 0.5 M TEOS dissolved in 15.0 mL of absolute ethanol, and the second (B) was a mixture of 0.5 M NH₄OH solution dissolved in 5.0 mL of ethanol and 3.0 mL of water. Then, solution B was added dropwise to solution A at a rate of 0.2 mL min⁻¹ and stirred for 3 h at room temperature. At the end of the reaction, silica nanoparticles were obtained in suspension. The TEOS/ethanol molar ratios were 0.03, 0.07 and 1.0.

In the CI method, chemically modified silica nanoparticles (S_NCI) were prepared using TEOS/SiCl₄ at molar ratios ranging from 0.1 - 8.0. The CI followed the same steps as the SG method but included the addition of SiCl₄ to mixtures A and B 3 h after the beginning of the reaction, which was followed by additional stirring for 1 h. In the Da method, hybrid nanosilicas (S_NDa) were obtained by the addition of ODA, which was previously dissolved in 15 mL of ethanol, stirred for 1 h at room temperature and mixed with TEOS in solution A. The Pu and Tw methods were used to synthesize the hybrid nanosilicas S_NPu and S_NTw , respectively, using Pluronic®L-31 and Tween®80. The amount of surfactants used in the syntheses of the hybrid materials was 0.0028 and 0.0056 mol for comparative purposes.

2.2.1 Synthesis of mixed-structure silicas using the sol-gel process

In this procedure, similar solutions (A and B) were prepared using the same steps performed during the synthesis of silica nanoparticles using methods SG, Cl, Da, Pu, and Tw. However, in the first solution (A), 0.2 g of Sylopol-948 (commercial microscale silica (S_M)) was mixed with 15.0 mL of absolute ethanol for 0.5 h. Then, 0.5 M TEOS was dissolved in solution A, which was then stirred for 1 h at room temperature. Subsequently, solution B was added dropwise to solution A at a rate of 0.2 mL min⁻¹ and stirred for 3 h at room temperature. At the end of the reaction, a suspension of mixed-structure silica $(S_M S_N)$ was obtained by the formation and growth of monodisperse nanosilicas on the surface of S_M . Chemically modified mixed-structure silicas were prepared with SiCl₄ and denoted by S_MS_NCl; hybrid mixed-structure silicas resulting from syntheses with ODA, Pluronic®L-31 and Twenn®80 were labeled as $S_M S_N Da$, $S_M S_N Pu$, and $S_M S_N Tw$, respectively.

The dispersions of the nanoscale and mixed-structure microscale silicas were centrifuged at 13,300 rpm for 30 minutes. Then, the samples were washed three times with ethanol (3 \times 20.0 mL). Lastly, the nanosilica particles were dried at 110 °C in an oven for 24 h and milled to obtain an extremely fine powder (approximately 50 μm in diameter). Scheme S1 depicts the steps involved in the synthesis of the

Page 3 of 12 RSC Advances

RSC Advances ARTICLE

nanosilica particles and mixed silicas. For example, $S_M S_N 7 C150$ refers to $S_M S_N C1$ prepared with a TEOS/ethanol molar ratio of 0.07 and a TEOS/SiCl₄ molar ratio of 5.0 (Scheme S1b), and $S_M S_N 7 Da28$ refers to $S_M S_N Da$ prepared with a TEOS/ethanol molar ratio of 0.07 and an ODA molar amount of 0.0028 (Scheme S1d). A nested design²⁸ was used as the experimental approach for the syntheses of the silica samples. Details of the preparation are provided in Scheme S2.

2.3 Characterization

Nitrogen adsorption isotherms were measured on a Micromeritics TriStar II 3020 in the partial pressure range of $0.01 < P \cdot P_0^{-1} < 0.25$. The specific surface area for each sample (SBET) was calculated using the Brunauer-Emmett-Teller method (BET), 29 and the pore diameter (Dp $_{\text{BJH}}$) and pore volume (Vp_{BIH}) were calculated using the cumulative desorption curve by the Barrett-Joyner-Halenda (BJH) algorithm.³⁰ Dynamic light scattering (DLS) measurements were performed on the samples in the liquid phase using a Zetasizer-Nano ZS90 (Malvern Instruments). The zeta potentials (ZP) of the particles in dispersion (approximately 10 mg.L⁻¹) were measured using a Zetamaster (Malvern Instruments). The chloride distributions of the S_NCl and S_MS_NCl particles were obtained using a scanning electron microscopyenergy dispersive X-ray spectroscopy (SEM-EDX) on a JEOL JSM-5800 with an accelerating potential of 20 kV. Thermogravimetric analyses (TGA) were performed on an SDT Q600 thermal analyzer Q20 (TA Instruments) at a scanning rate of 20 °C·min⁻¹ from 25 to 600 °C. X-ray diffraction (XRD) measurements were obtained on a Rigaku DMAX 2200 equipped with a Cu-Kα (λ of 1.54 Å) tube. Scanning electron microscopy (SEM) images were collected on an EVO-50 (Carl Zeiss, Inc.) equipped with an Everhart-Thornley secondary electron (ETSE) detector at 0.2 to 30 kV. Transmission Electronic Microscopy (TEM) images were obtained using a JEOL JEM-2010 transmission electron microscope operating at 200 kV with a lattice resolution of 0.14 nm and a point-topoint resolution of 0.25 nm.

A diffuse reflectance infrared Fourier transmission spectroscopy (DRIFTS) was performed on a Shimadzu FTIR 8300 spectrometer equipped with a diffuse reflectance accessory. All spectra were collected in the frequency range of 4000 to 400 cm⁻¹ in the absorbance mode at a resolution of 4 cm⁻¹. Approximately 600 scans were averaged and rationed against the same number of scans for the background (finely ground KBr, FTIR grade) to obtain a suitable signal-to-noise ratio. Multiple spectra (triplicate) were acquired for each sample to determine the reproducibility. Sample preparation for DRIFTS analysis consisted of the grinding of a mixture of KBr and silica sample in appropriate weight proportions to spectral absorbance, after the mixture was pelletized using a hydraulic press. OriginPro 8.5.0 SR1 (Northampton, MA 01060 USA, OriginLab Corporation) was used to assign the wavenumber using the Screen Reader tool. The characteristic spectral bands of the harmonic vibrations of the silica material networks $[v_{as(Si-O(-Si))}]$ were studied using the FT-IR method in the region of 1300-1000 cm⁻¹. ^{18, 31} The structural parameters,

such as the percentage of six-fold siloxane rings ((SiO) $_6$), longitudinal-optical (LO) percentage (% LO), and proportion of silanol groups % (Si-OH) in the silica network, were estimated using Equations (S1), (S2), and (S3) according to the literature. $^{16,\,31}$

Small-angle X-ray scattering (SAXS) measurements were performed on the D1B-SAXS1 beamline at the National Synchrotron Light Laboratory (LNLS, Campinas, Brazil). The scattered X-ray beam presented a wavelength (λ) of 1.488 Å and was detected on a Pilatus 300 k detector. The scattering intensity I(q) was plotted as a function of the modulus of the scattering vector q ($q = 4\pi/\lambda$) sin θ ; 2θ = scattering angle). To reduce the limit detection, the incident beam was detected at two different sample-to-detector distances (0.5 and 3.0 m) to extend the q vector collecting range (from 0.04 nm⁻¹ to 5 nm⁻¹ 1). The SAXS scattering patterns from the two distance measurements were merged using Wolfram Mathematica®9 to obtain the resulting merged SAXS profiles for each sample in triplicate. Silver behenate was measured under the same conditions to calibrate the sample-to-detector distance, detector tilt and direct beam position. Each powder sample was prepared in triplicate, and they had been previously fixed in a sampler (covered by Kapton™ foil). Using Beaucage's model, 32, 33 a multi-level unified fit was used to establish multihierarchical structures of the particles from the scattering data. $^{18, 34}$ The I(q) vs q scattering profiles were fit by the Irena evaluation routine,³⁵ and the equation can be used to fit the data for each structural region as follows:

$$\begin{split} &I(q) \simeq \mathbf{B}_{L} \exp \left(-q^{2} \cdot \frac{\mathbf{R}\mathbf{g}_{M}^{2}}{3}\right) \times \left\{\left[erf\left(q \cdot \frac{\mathbf{R}\mathbf{g}_{L}}{\sqrt{6}}\right)\right]^{3} / q\right\}^{\mathbf{P}_{L}} + \mathbf{G}_{M} \exp \left(-q^{2} \cdot \frac{\mathbf{R}\mathbf{g}_{M}^{2}}{3}\right) + \\ &\mathbf{B}_{M} \exp \left(-q^{2} \cdot \frac{\mathbf{R}\mathbf{g}_{H}^{2}}{3}\right) \times \left\{\left[erf\left(q \cdot \frac{\mathbf{R}\mathbf{g}_{M}}{\sqrt{6}}\right)\right]^{3} / q\right\}^{\mathbf{P}_{M}} + \mathbf{G}_{H} \exp \left(-q^{2} \cdot \frac{\mathbf{R}\mathbf{g}_{H}^{2}}{3}\right) + \mathbf{B}_{H} \times \\ &\left\{\left[erf\left(q \cdot \frac{\mathbf{R}\mathbf{g}_{H}}{\sqrt{6}}\right)\right]^{3} / q\right\}^{\mathbf{P}_{H}} \end{split} \tag{1}$$

where Rg is the radius of gyration for the particles in each region, in which the subscript indicates the structural region of the SAXS scattering profile, i.e., Rg_L for the low-q region, Rg_M for the mid-q region and Rg_H for the high-q region; Rp is the radius of the particle; G is the Guinier prefactor; B is a multiplicative factor specific to the type of power-law regime; and P is defined based on the regime in which the power-law exponent decays, i.e., $P_H = 4.0$ in the high-q region. The principal parameters obtained from Equation (1) are the power-law regime (P) and the radius of gyration of the particles (Rg). The particle radius (Rp) was calculated as Rp = Rg× (5/3)^(1/2).

2.4 Multivariate data processing

Principal component analysis (PCA) is a statistical multivariate technique used to analyze the variance-covariance structure of a set of data.²¹ It projects data in a reduced hyperspace defined by a set of orthogonal vectors known as principal components.³⁶ These are non-correlated linear combinations of the original variables ordered by the amount of variance

ARTICLE RSC Advances

explained in the component directions.³⁶ Thus, the first principal component has the largest variance, the second principal component has the second largest variance, and so on. This method reduces the complexity of the input variables when addressing large datasets. The data are transformed into a small number of principal components (PCs).³⁷ These PCs allow for the variability in the dataset to be studied in parts and permit a different interpretation that is occasionally not possible from direct observation of the dataset.²¹

The coefficients of variables used to determine the principal components are stored in the loading matrix. Given a set of I samples and J variables arranged in a two-dimensional matrix X ($I \times J$), the loadings are coefficients for each PC and can be calculated using the singular value decomposition (SVD) of the covariance matrix C as follows:

$$C = \frac{X^{\mathrm{T}}X}{I-1} = LS^{2}L^{\mathrm{T}} = Z\Lambda Z^{\mathrm{T}}$$
 (2)

where Z $(J \times J)$ is an orthogonal matrix; S $(J \times J)$ is a diagonal matrix with the nonzero singular values on its diagonal; L $(J \times J)$ is the loading matrix, which collects the coefficients of the J variables for defining the j-th principal component in each j-th column (eigenvector); and Λ is the diagonal matrix, which contains the nonnegative eigenvalues of decreasing magnitude $(\lambda_1 \ge \lambda_2 \ge ... \lambda_J \ge 0)$.

Hierarchical cluster analysis (HCA) detects similarities in the structural characteristics between samples and defines

groups, clusters, or hierarchies in data based on sample similarities. ^{22, 36} Similarities among samples are estimated by measuring the distances between points (samples) in the measurement space; similar samples are characterized by small distances, and vice versa for dissimilar samples. ³⁶ HCA calculates the distances using a defined metric, such as the Euclidean distance or Manhattan distance, ³⁸ and the results are typically displayed as a dendrogram. The dendrogram depicts the merging of samples into clusters at various stages of analysis and the similarities at which the clusters merge, where the clustering is displayed hierarchically. ²²

All the FT-IR spectra in the region of 2000 – 400 cm⁻¹ and the SAXS profiles in the region of 0.04 to 5 nm⁻¹ were treated by multivariate analysis tools using hierarchical cluster analysis (HCA) and principal component analysis (PCA).³⁹ The mean centered data and the standard normal variate (SNV) were used as pre-processing tools for the multivariate analyses.²⁰ MATLAB® 7.11.0 software (The Math Works, Natick, MA, USA) and the PLS-Toolbox 6.0 package (Eigenvector Research, Copenhagen, Denmark) were used.

3 Results and discussion

The surface and textural characterizations of the silical nanoparticles and the mixed-structured silicals were performed using nitrogen porosimetry. Fig. 1 illustrates one typical nitrogen adsorption/desorption isotherm of synthesized $S_N 7Da28$ and $S_M S_N 7Da28$ using the ODA. These materials display a type IV

Table 1 BET isotherm parameters (S_{BET} , V_p , and Dp_{BJH}) and multi-organizational parameters of the SAXS profiles (Rg_H , $P_H = 4$, Rg_M and P_M , and P_L) obtained through a unified fit, and the correlation between the structural parameters %(SiO)₆, %LO and (%Si-OH) is derived by deconvolution of the FT-IR spectra.

Sample	S _{BET}	Vр _{вјн}	Dр _{вJН} (nm)	High- <i>q</i> region		Mid-q region			Low-q region	(SiO) ₆	LO	(Si-OH)
	(m ² .g ⁻¹)	(cm ³ .g ⁻¹)		Rg_H (nm)	Rp _H ^{b)} (nm)	Rg _M (nm)	Rр_м (nm)	P _M ^{c)}	P_L	(%)	(%)	(%)
S _M	272	1.47	15.7	1.1	1.4	5.7	7.4	4.2	2.3	42.6	73.8	12.5
S _N 7	369	0.96	9.3	0.4	0.5	7.3	9.4	3.9	2.8	23.7	66.3	11.6
$S_M S_N 7$	313	0.87	9.4	0.4	0.5	7.5	9.7	3.9	2.9	49.9	51.0	13.1
S _N 7Cl30 ^{d)}	714	0.17	2.6	0.8	1.0	3.0	3.9	4.0	3.8	65.9	56.2	16.3
S _N 7Cl50	522	0.11	2.6	0.4	0.5	2.4	3.0	4.0	3.8	46.9	51.5	20.0
$S_M S_N 7 Cl30$	567	0.25	4.3	0.4	0.6	5.4	7.0	3.6	3.3	51.9	45.9	20.9
$S_M S_N 7 CI 50$	231	0.74	9.5	0.8	1.1	5.7	7.4	4.0	3.3	50.3	47.3	18.1
S _N 7Da28	286	0.42	5.0	0.3	0.4	8.2	10.6	3.6	3.0	26.1	64.5	10.8
S _M S _N 7Da28	179	0.35	7.1	0.3	0.3	10.3	13.3	3.9	2.5	45.4	41.1	15.6
S _M S _N 7Da56	212	0.72	10.1	2.0	2.6	6.4	8.3	3.7	2.2	69.0	42.7	21.1
S _N 7Tw28	39	0.17	14.6	0.9	1.2	22.2	28.6	3.9	2.4	34.8	45.2	14.9
$S_M S_N 7 Tw 28$	150	0.60	12.6	0.8	1.0	8.0	10.3	3.6	2.4	44.1	38.9	29.2
$S_M S_N 7Tw56$	127	0.64	16.4	0.7	0.8	16.9	21.8	3.9	1.7	47.5	36.1	10.4
S _N 7Pu28	204	1.21	19.5	0.9	1.2	10.9	14.1	3.7	2.7	47.1	52.4	8.2
S _M S _N 7Pu28	153	0.60	11.9	0.7	0.8	6.6	8.5	3.5	2.2	55.2	40.0	3.5
S _M S _N 7Pu56	138	0.75	14.2	0.4	0.5	13.8	17.8	4.0	2.8	53.6	37.2	12.4

a) Rg is the radius of gyration of the particles in each region: Rg_H in the high-q region, Rg_L in the low-q region, and Rg_M in the mid-q region; b) and c) Rp and P are the radius of the particle and the power-law exponent decay extracted in each region, respectively, $P_H = 4.0$ at high-q region; and d) Cl30 corresponds to a TEOS/SiCl₄ molar ratio of 3.0.

ARTICLE

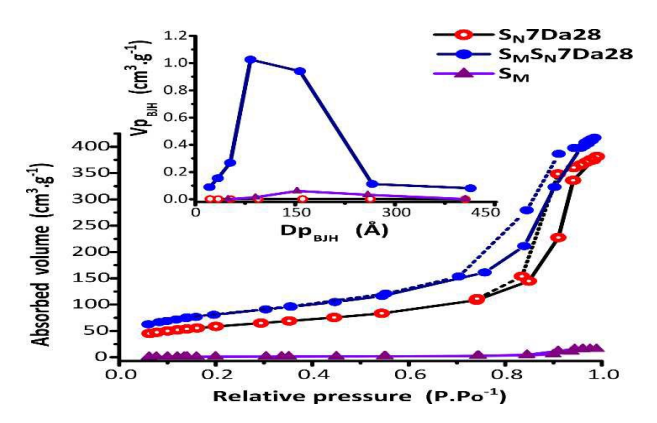


Fig. 1 Comparison of the N_2 adsorption-desorption isotherms between $S_N Da$, $S_M S_N Da$, and S_M . Inset: BJH pore size distributions (Dp_{BJH}).

isotherm and exhibit hysteresis, which is typical of mesoporous materials. ⁴⁰ For clarity, only data concerning the specific surface area (S_{BET}) , ²⁹ specific pore volume (Vp_{BJH}) , and pore diameter (Dp_{BJH}) of the materials using a TEOS/ethanol molar ratio of 0.07 are presented in Table 1. The results of all five methods for different TEOS/ethanol and TEOS/SiCl₄ molar ratios and the amount (mol) and type of surfactant are listed in Table S1.

From Table 1, functionalized nanosilicas (S_N7Cl50 and S_N7Cl30) achieved larger surface areas ($522 - 714 \text{ m}^2.\text{g}^{-1}$, respectively, Table 1) with smaller pore sizes. The presence of organic groups from the surfactants on the silica nanoparticles decreases the specific surface area (e.g., compare S_N7 , 369 $\text{m}^2.\text{g}^{-1}$ and S_N7Da28 , $286 \text{ m}^2.\text{g}^{-1}$ with S_N7Pu28 , $204 \text{ m}^2.\text{g}^{-1}$). The synthesized nanosilica particles have an effect on the surface

characteristics of S_M . The specific surface area of S_M increases, and the pore shape changes due to the presence of nano- or functionalized nanosilicas (e.g., compare S_MS_N7 , 313 $m^2.g^{-1}$, S_MS_N7Cl30 , 567 $m^2.g^{-1}$ with S_M , 272 $m^2.g^{-1}$). 18 Otherwise, S_{BET} decreases for hybrid mixed-structure silicas when the surfactant concentration is enhanced (from S_MS_N7Tw28 , 150 $m^2.g^{-1}$ to S_MS_N7Tw56 , 127 $m^2.g^{-1}$). Eltejaei *et al.* 41 reported that large molecular surfactants affect S_{BET} .

The presence of organic molecules in the hybrid particles was verified using TG analysis, as indicated in Fig. S1a in the Supplementary Information. The decrease in mass between 363 °C and 476 °C was 17% for $S_M S_N 7 Pu 28$, which may be due to the thermal decomposition of organic molecules from Pluronic®L-31. XRD analysis was used to study the amorphous structure of the hybrid mixed-structure silicas, as indicated in Fig. S1b. The diffractograms of the hybrid particles presented a halo in the 2θ region between $18 - 27^{\circ}$, which is characteristic of an amorphous silica structure. 42 The particle diameter (d_{XRD}) estimated by Scherer's equation varied between 3.6 - 3.9 Å. The results indicated a shift towards higher 20 angles for the hybrid systems compared to that of S_M. This behavior suggested that the incorporation of organic molecules resulted in the formation of a compact and denser silica particle, which is in agreement with the results obtained by Yu et al. 43

3.1 Molecular structural characteristics

The FT-IR spectra of the synthesized materials have a few common bands, which display only slight changes in their relative intensities, as depicted in Fig. 2. The proposed band assignments are summarized in Table S2 and are based on values from the literature. 16, 31, 44

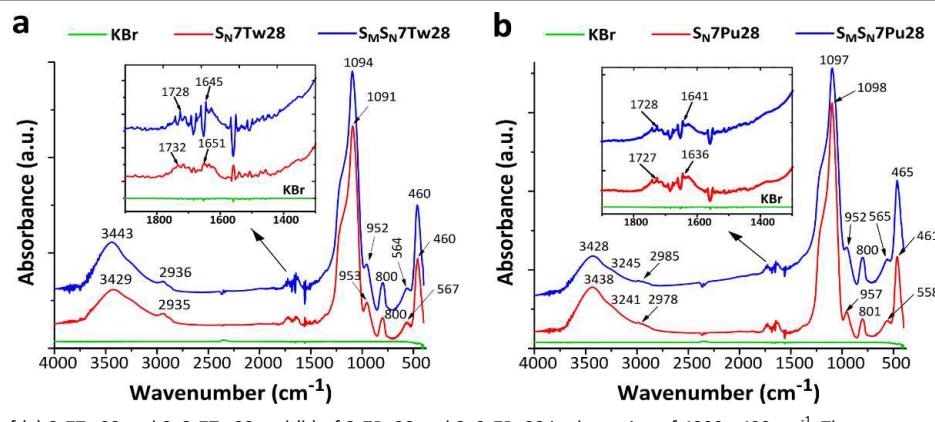


Fig. 2 FT-IR spectra of (a) $S_N 7 Tw28$ and $S_M S_N 7 Tw28$ and (b) of $S_N 7 Pu28$ and $S_M S_N 7 Pu28$ in the region of 4000 - 400 cm⁻¹. The spectra were normalized to the maximum of the $v_{as}(Si-O(-Si))$ band. Resolution: 4 cm⁻¹

ARTICLE

Based on Fig. 2a, the FT-IR spectra of S_N7Tw28 and S_MS_N7Tw28 exhibit an absorption band at $1732~cm^{-1}$ and $1728~cm^{-1}$, respectively, attributed to the symmetric stretching C=O of the ester bond. $^{43,~45}$ The two bands at $1651~cm^{-1}$ (S_N7Tw28) and $1645~cm^{-1}$ (S_MS_N7Tw28) are attributed to -COO. 46 The FT-IR spectra of S_N7Pu28 and S_MS_N7Pu28 are illustrated in Fig. 2b, which present certain bands equal to the synthesized silicas using Tween®80. The band assignment was compared with previously published reports from Yu et~al. Liu et~al. and Macher et~al. Fig. 2 illustrates that the bands and shows that their intensities vary based on each system.

The spectra provide relevant information on the arrangements of the structural units ((SiO)₄) in the silica network through the vibrational modes of [$v_{as(Si-O(-Si))}$] found in the 1300 – 1000 cm⁻¹ region.^{15, 16} The structural parameters were expressed as a six-fold ring ((SiO)₆) and longitudinal-optical (LO) mode percentages as well as the proportion of silanol groups. These parameters were estimated using Equations (S1), (S2), and (S3).^{16, 31} The (SiO)₆, (LO), and (Si-OH) percentages are summarized in Table 1.

Nanosilicas (S_N) tend to organize themselves into cyclical siloxane arrangements, (S_{IO})₄ (23.7% (S_{IO})₆), which are tensioned structures ($\theta \approx 125^\circ$). When silica nanoparticles interact with a halogen, such as CI, or an organic group from a molecular surfactant (ODA, Tween®80 and Pluronic®L-31), they form functionalized (S_N CI) or hybrid (S_N Da, S_N Tw e S_N Pu) nanosilicas. Therefore, the silica network is modified to the most thermodynamically stable structure 47 with a larger number of six-member cyclic units (26.1 to 65.9% (S_{IO})₆), as indicated in Table 1. The longitudinal vibrational modes become sensitive to the incorporation of the CI atoms and

organic groups; 48 hence, the percentage of LO varied from 45.1 to 64.5%.

The mixed-structure materials, either functional (S_MS_NCI) or hybrid ($S_M S_N Da$, $S_M S_N Tw$, and $S_M S_N Pu$), revealed that the structure of the silica matrix interacted with the silanol groups on the surface of $S_M S_{N_{\rm c}}$ as indicated in Table 1. These interactions depended on the synthesis method and generated materials with different molecular properties (42.6 - 69% of (SiO)₆, 38.9 -47.3% of LO, and 15.6 - 29.2% of Si-OH). The larger organic molecular groups of the surfactants demonstrate a tendency to form six-membered rings in previous studies, which most likely allows them to be accommodated within the network. 16, 31 The presence of distinct groups (such as C=O, -CH₂, C=C, and Si-Cl) on the surface of S_M increased the amount of six-member siloxane rings ((SiO)₆) by 38%, raised the LO mode by 23% and increased the quantity of Si-OH by 37%. Additionally, an increase in the organic groups decreased the Si-O-Si angle in the silica network of the hybrid materials. which reduced the long-range Coulomb interactions and displaced the LO components to higher wavenumbers. 48, 49

3.2 Multi-scale organization and fractal structure

For each sample, the multi-hierarchical organization of the particles, radius of gyration (R_g), organizational state of the fractals of the particles ($I\!\!\!/_L$ for the low-q region and $I\!\!\!/_{I\!\!\!/_L}$ in the high-q region) and shape were investigated using the unified approach $^{32,~33}$ in the Guinier and power-law regions. Fig. 3 depicts the experimental SAXS curves (Δ , O, and \Box) and their corresponding best fits (solid lines), with Sylopol-948 ($I\!\!\!\!/_{SM}$), functionalized nanosilica particles ($I\!\!\!/_{SN}$ 7CI30), hybrid silica nanoparticles ($I\!\!\!/_{SN}$ 7CI30 and $I\!\!\!/_{SN}$ 7CI30 and $I\!\!\!/_{SN}$ 7CI30 as examples.

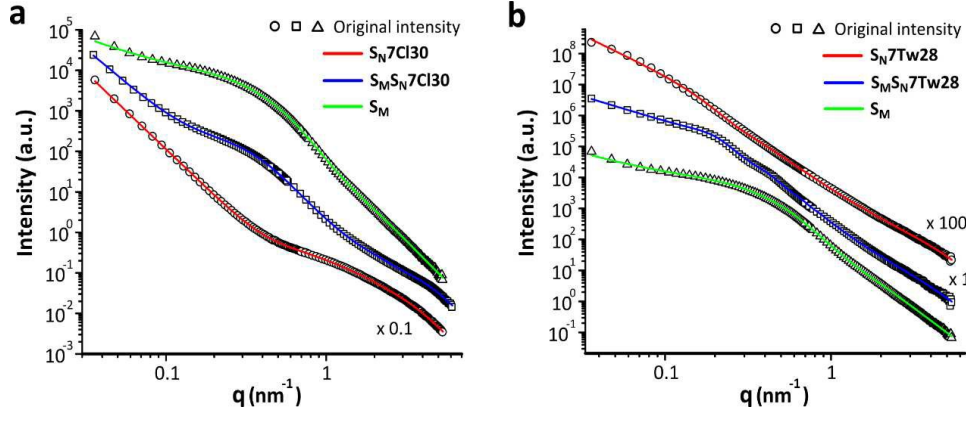


Fig. 3 (a) SAXS profiles of S_M (Δ , green), S_N 7Cl30 (O, red), and S_M S $_N$ 7Cl30 (\Box , blue); and (b) SAXS profiles of S_M (Δ , green), S_N 7Tw28 (O, red), and S_M S $_N$ 7Tw28 (\Box , blue). The corresponding fits (solid lines) assume a homogeneous spherical model.

ARTICLE

Based on Fig. 3, the unified set of the SAXS data reveals that the samples are arranged in a multi-hierarchical structure. Using Beaucage's model,^{32, 33} it was possible to establish a multi-hierarchical structure of the particles using Equation (1) to fit the data for each structural region. The results of the unified approach applied to the SAXS curves from the particles are provided in Table 1.

Based on Fig. 3a, smaller silica nanoparticles are obtained when $SiCl_4$ is used to chemically modify the surface of the nanosilicas (e.g., compare $S_N TCl30$, $Rp_M = 3.9$ nm and $S_N TCl50$, 3.0 nm with $S_N T$, 9.4 nm, see Table 1). We observed that the size of the nanosilica particles increases as the $SiCl_4$ concentration increases; simultaneously, the surface potential decreases, i.e., $S_N TCl50$ reaches a higher surface charge (ZP = -22.9 mV) compared to $S_N TCl30$ (ZP = -10.6 mV) when the $SiCl_4$ concentration is low (Table S3). Eventually, the repulsive barrier becomes large enough to prevent the coagulation (or further growth) of particles. Our data are in agreement with those obtained by Parfitt et al., SP Brinker et al., and Ma et al., if the sol contains particles that vary in size, i.e., smaller particles may aggregate with larger particles.

Furthermore, the incorporation of organic groups from surfactants on the surface of nanosilicas increases the size of the particles, as indicated in Fig. 3b (for example, $S_N TTw28$, $\mathbb{R}p_M = 28.6$ nm). However, it is possible that the organic groups may be trapped between the primary particles, thus forming a secondary particle size. Park *et al.*⁵⁵ reported that when more spherical particles have to be packed within the

same volume of solution at high polymer concentrations, the distance between the particles is further reduced. We observed that larger polymer chains increase the particle radii (e.g., compare $S_{\rm N}7{\rm Da}28,~10.6$ nm with $S_{\rm N}7{\rm Tw}28,~28.6$ nm), and the organizational structure of clusters is predominately mass fractals based on the results of the power law, $(1.7 < P_L < 3.0).$ The size distribution of the particles influences the textural characteristics of the materials: if the particles increase in size (Rp), $S_{\rm BET}$ decreases. 18

The growth of the silica nanoparticles on the surface of S_{M} , which resulted in a mixed-structure silica, affected the organizational structure of the functionalized mixed-structure silicas (S_MS_NCI) by generating surface fractals (3.3 < P_L <3.8). Regarding the hybrid mixed-structure silicas, the radii of the aggregated particles increased due to the presence of nanosilica particles, and the volume and pore diameter decreased (e.g., compare S_MS_N7Pu56 , Rp_M = 17.8 nm, Vp_{BJH} = 0.75 cm³.g¹¹, Dp $_{BJH}$ = 14.7 nm and S_MS_N5Tw56 , 21.8 nm, 0.64 cm³.g¹¹, 16.4 nm with S_M , 7.4 nm, 1.47 cm³.g¹¹, 15.7 nm).

3.3 Multivariate correlation analysis between FT-IR and SAXS

The FT-IR spectra and SAXS scattering curves of the samples were subjected to multivariate analyses to determine the most important information and significant correlations between the molecular structural characteristics and the multi-hierarchical organization of the particles. Fig. 4a depicts the dendrogram obtained from the FT-IR spectra whereas Fig. 4b presents the scatter profiles.

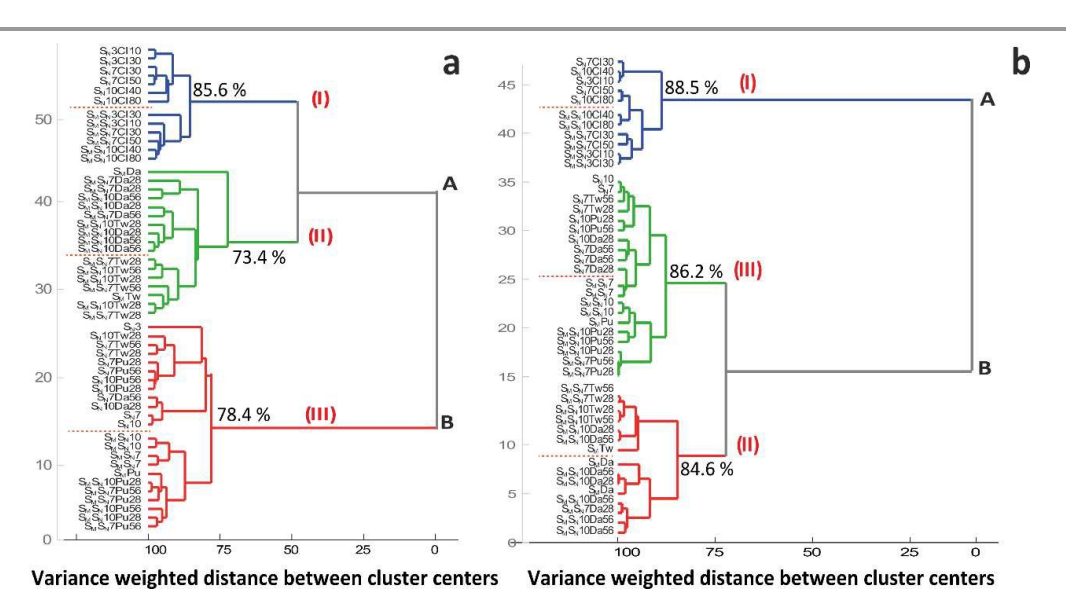


Fig. 4. Dendrogram obtained from HCA applied to the FT-IR spectra (a) and the SAXS profiles (b) for all 28 samples.

ARTICLE

Hierarchical clustering analysis (HCA) was applied to the FT-IR spectra in the region of 2000-400 cm $^{-1}$ and demonstrated that the materials are divided into two primary groups, A and B, as indicated in Fig. 4a. Group A is further divided into two classes, class I, which consists of particles functionalized with chlorine atoms on the surface (similarity of 85.6 %), and class II, which is composed of hybrid mixed-silicas obtained from ODA and Tween $^{\circ}$ 80 (similarity of 73.4%). Group B consists of nanosilicas, hybrid nanosilica particles, mixed-structure silicas ($S_{\rm M}S_{\rm N}$), and the hybrid mixed-structure ($S_{\rm M}S_{\rm N}$ Pu) using Pluronic $^{\circ}$ L-31, which has a similarity of 78.4%.

In parallel, as indicated in Fig. 4b, HCA of the SAXS data revealed that the multi-scale structures of these materials are different and can be divided into two primary groups, A and B. Group A consists of the functionalized particles (nano- and mixed-structure) with an 88.5 % similarity. Group B is divided into two classes. Class II, with an 84.6 % similarity, consists of the hybrid mixed-structure silicas using ODA and Tween®80; this class is in agreement with the FT-IR spectra dendrogram. Class III, with an 86.2 % similarity, consists of hybrid silica nanoparticles $\rm S_M S_N$, and $\rm S_M S_N Pu$ using Pluronic®L-31. This class is in agreement with class III (78.4%) from the FT-IR spectra, as indicated in Fig. 4a.

The molecular structural characteristics from the FT-IR spectra and the multi-scale organizational structure and fractal from the SAXS scattering (Figs. 4a and 4b, respectively) allowed us to classify all of the synthesized materials into classes I, II, and III with good agreement. Essentially, the data suggest that the separation of groups (A and B) for the SAXS profiles is based on the incorporation of organic groups in the

silica network of particles and the organizational structure of aggregates in the low-q region. Functionalized particles with chlorine atoms (S_NCl and S_MS_NCl) depicted higher similarities (85.6% and 88.5%) and were separated from the other classes (II and III) because these particles organized as mass fractals (3.0 < P_L < 3.8).³³ 3.4 Assessment of structural differences by PCAPrincipal component analysis (PCA) presents the treatment of the FT-IR spectra and SAXS curves in a two-dimensional space to verify the separation of groups of materials based on their characteristics, as depicted in Fig. 5a and Fig. 5b, respectively. 20,22

Based on Fig. 5a, 89.5% of the variations in the FT-IR spectra in the region of 2000 - 400 cm $^{-1}$ were explained by analyses of the principal component (PC1). In this case, the samples in group A, which are divided into class I and class II (similar to Fig. 4a), are represented by negative values of PC1 whereas the samples in group B are denoted by positive values. This behavior can be attributed to two factors as follows: (i) the percentage of silanol groups 10.4 < Si-OH < 29.2% on the surfaces of the particles from classes I and II are greater than those on the surfaces of the particles in class III (shown in Table 1); 16 and (ii) a smaller peak intensity [v_{(OH)}] at 3416 - 3443 cm $^{-1}$ in the spectra of the functionalized particles resulting from the reaction of the surface hydroxyl groups on S_{N} with SiCl_4 . 56

The loading graph for PC2, with a 7% variation, was better suited to separate materials with organic groups incorporated into the silica network as positive values on the PC2 axis, as indicated in Fig. 5a. The presence of organic groups in the

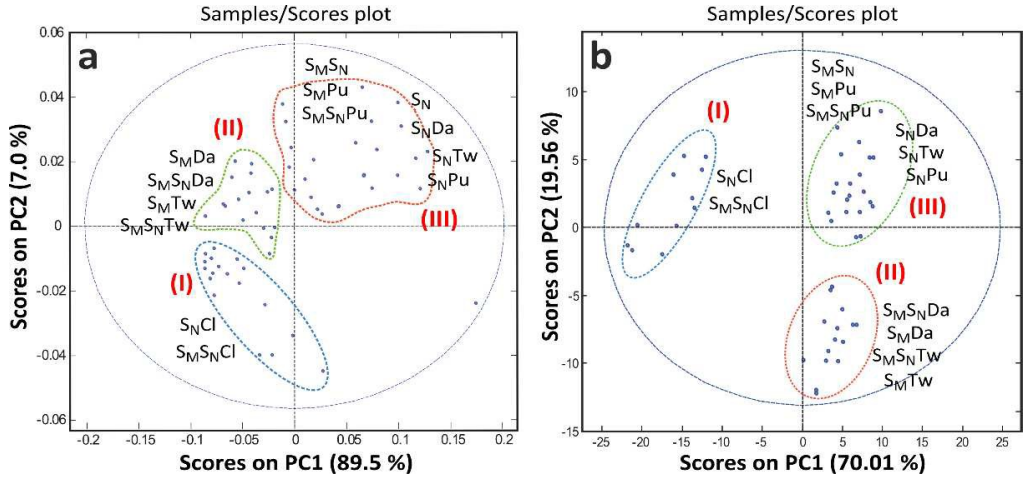


Fig. 5 Scores obtained from PCA applied to the FT-IR spectra (a) and SAXS profiles (b) for the data from all samples (N = 28).

ARTICLE

hybrid mixed-structure silica decreased Dp_{BJH} and S_{BET} (Table 1). It appears that the organic molecules interact with both the surface and the pores of S_M ; they fill the empty spaces between the nanosilicas and the microparticles, thus creating a more compact and denser silica, which decreases the amount of pores available for the N_2 gas adsorption. Due to the pore blockage, the pore size distribution of S_M becomes larger, and Dp_{BJH} decreases (e.g., compare Dp_{BJH} for S_MS_N7Da28 , 7.1 nm, S_MS_N7Tw28 , 12.6 nm, and S_MS_N7Pu28 , 11.9 nm with that of S_M , 15.7 nm).

Based on the SAXS curves, the loading plot for PC1 (Fig. 5b) reveals that 70.0% of the variation in the scattering vector (q) is given by the organizational structure of the clusters. This separates the surface fractals (3.0 < P_L <3.8), i.e., S_MS_NCl and S_NCl in group A (Class I), from the mass fractals (1.7 < P_L < 2.8), i.e., nanosilicas, hybrid silica nanoparticles, mixed-structure silicas, and hybrid mixed-structure particles that belong to group B (classes II and III).

3.5 Effects of nanosilica particles on the morphological characteristics of mixed-structure silica

The TEM was used to evaluate the particle morphology and the sizes of the silica nanoparticles in the dispersions. High-magnification images (40,000×) of the nanosilicas, S_N , are depicted in Fig. 6a whereas S_N Pu is illustrated in Fig. 6b.

Based on Fig. 6, sol-gel synthesis influenced the morphology of the nanosilica particles. S_N consists of spherical nanosilica particles that are approximately 20 nm in diameter and exhibit a tendency to agglomerate whereas the S_N Pu sample contains smaller deformed monodispersed particles. As indicated in Fig. 6c, S_M is a micrometric silica with a rough surface, which is consistent with the hierarchical parameter (P_L \approx 2.3) obtained from the SAXS data (Table 1).

It is possible to evaluate the morphology and investigate the effects of incorporating spherical nanoparticles of silica on the S_M surface. At high magnification, Fig. 6d illustrates the surface of $S_M S_N 7 T w 28$ with a large number of spherical hybrid

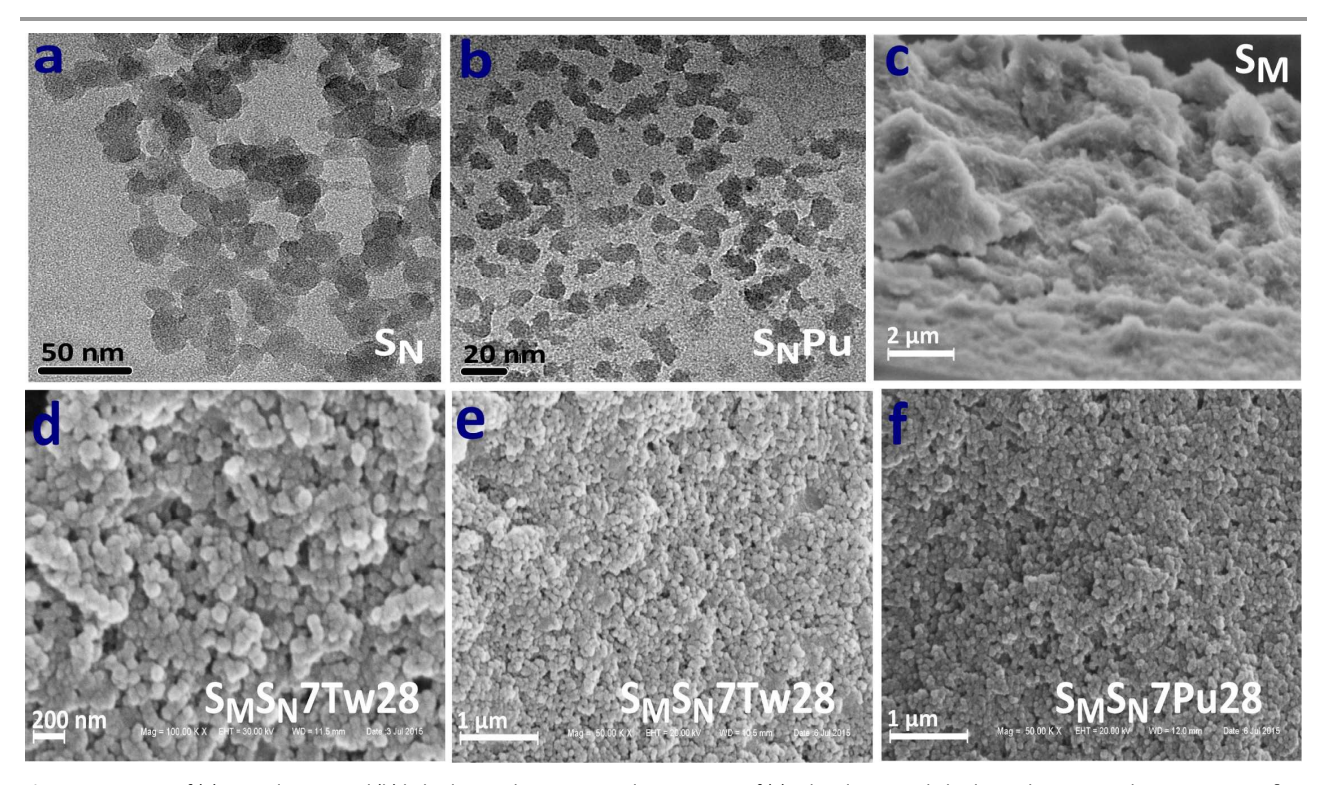


Fig. 6 TEM images of (a) nanosilica, S_N , and (b) hybrid nanosilicas, S_N Pu; and SEM images of (c) Sylopol-948, S_M , hybrid mixed-structure silicas using Tween®80 (d and e), and Pluronic®L-31 (f).

ARTICLE

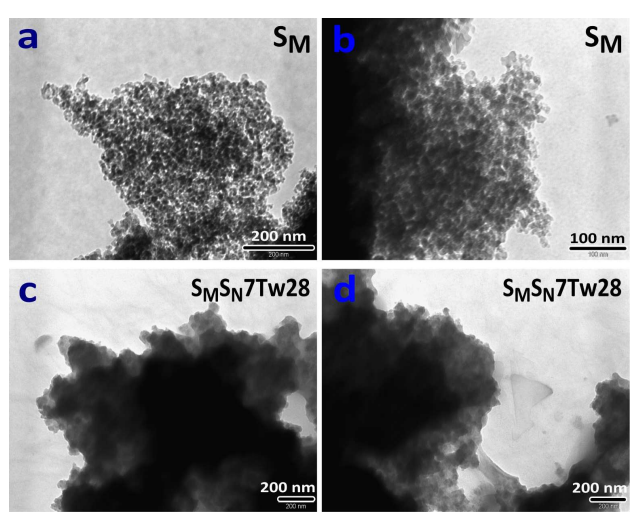


Fig. 7 TEM images of Sylopol-948, S_M (a and b) and hybrid mixed-structure silica using Tween 880 , S_MS_N7Tw28 (c and d).

 S_MS_N7Tw28 with a large number of spherical hybrid nanoparticles of silica that favor aggregation. Fig. 6e (low magnification) reveals that S_MS_N7Tw28 , which used Tween®80, exhibits a larger surface that is completely covered by nanosilica particles. Furthermore, a similar behavior was observed with S_MS_N7Pu28 , which used Pluronic®L-31 (Fig. 6f). The small nanoparticles of silica on the surface of S_MS_N7Tw28 compared with those on the surface of S_MS_N7Pu28 are most likely due to the Tween®80 possessing polymer chains that are larger and more complex than the Pluronic®L-31, as indicated in the SAXS results (Rp_H , Table 1).

Based on Fig. 6e and Fig. 6f, it is possible to synthesize hybrid mixed silicas from the growth and self-assembly of synthesized nanosilicas on the surfaces of microscale particles, thus allowing for the formation of a mixed-single system.

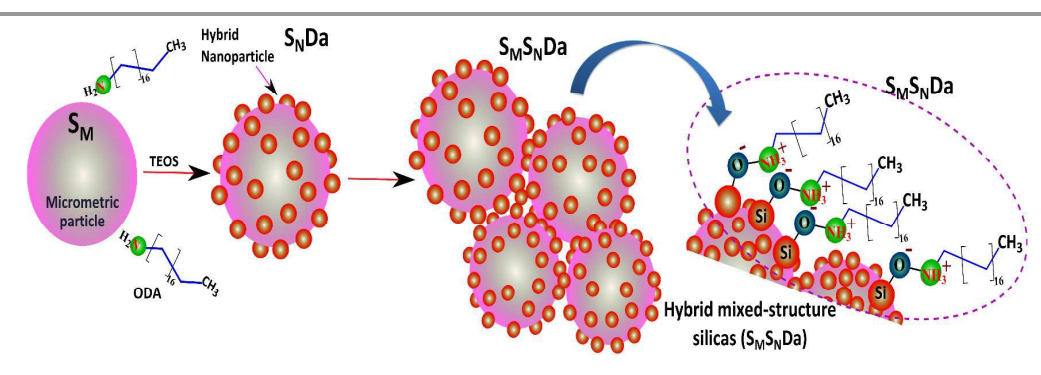
The above morphological evidence, particularly the size and shape of the nanosilicas, suggests that nanosilicas played a role in enhancing the surface heterogeneity of S_M while also forming pores, as demonstrated by the textural characteristics (Table 1).

Based on Fig. 7a and Fig. 7b, the large pore diameters ($Dp_{BJH}=15.7$ nm) of S_M can be observed as white voids, in agreement with the textural characterizations. It is possible to observe the existence of porosity in $S_M S_N Tw28$, as displayed in Fig. 7c and Fig. 7d, although their pores are partially hidden by the presence of the surfactant, Tween®80. The $S_M S_N Tw28$ porosity can be better observed in the SEM image, as indicated in Fig. 6d. $S_M S_N Tw28$ is a relatively more compact silica than S_M .

Based on the TEM and SEM results, the model depicted in Scheme 1 was proposed to describe the formation of hybrid mixed-structure silicas. The model considers the interactions between the silica nanoparticles (S_NDa) and the commercial micrometer silica S_M and uses a single method of synthesis as an example.

Conclusions

The molecular structural characteristics (FT-IR spectra) and multi-scale organizational structure and fractal (SAXS scattering) properties were correlated with the results of multivariate analyses, including HCA and PCA. It was determined that only two principal components accounted for over 96.5 and 89.7% of variance (FT-IR and SAXS, respectively) within the sample set. The aspects that most influenced the separation of samples by groups were: (i) the incorporation of organic molecules in the silica network of particles; (ii) the organizational fractal structure of aggregates at a low-q; and (iii) the percentage of silanol groups on the surface of particles. The functionalized particles with chlorine atoms depicted high degrees of similarity (85.6% from FT-IR spectra



Scheme 1. Suggested model for the formation of S_MS_NDa from S_NDa and S_M.

ARTICLE

and 88.5% from SAXS curves). As demonstrated in this study, FT-IR/SAXS/multivariate analysis showed excellent agreement in characterizing changes in the structural properties of mesoporous silica materials, and this new methodology can serve as a reliable and faster approach for practical applications that require high precision and accuracy.

Acknowledgements

This project was partially financed by the Conselho Nacional de Desenvolvimento Científico e Tecnológico (CNPq). Y.P. Moreno is grateful for the grant provided by CAPES. Furthermore, the authors would like to thank the LNLS (Project SAXS1-17056) for the SAXS beamline measurements as well as the Center for Nanoscience and Nanotechnology (CNANO) and the Electron Microscopy Center (CME) of UFRGS for the SEM measurements and the TEM measurements, respectively.

Notes and references

- L. Liu, R. Toledano, T. Danieli, J. Q. Zhang, J. M. Hu, D. Mandler, Chem. Commun., 2011, 47, 6909.
- 2 M. Wang, J. Han, H. Xiong, R. Guo, Y. Yin, ACS Appl. Mater. Interfaces, 2015, 7, 6909.
- 3 J. Moghal, J. Kobler, J. Sauer, J. Best, M. Gardener, A. R. Watt, G. Wakefield, ACS Appl. Mater. Interfaces, 2012, 4, 854
- 4 J. L. Silveira, S. R. Dib, A. M. Faria, *Analytical Sciences*, 2014, 30, 285.
- 5 L. B. Capeletti, L. F. de Oliveira, K. de A. Gonçalves, J. F. A de Oliveira, Â Saito, J. Kobarg, J. H. Z. dos Santos, M. B. Cardoso, Langmuir, 2014, 30, 7456.
- 6 P. A. Bazuła, P. M. Arnal, C. Galeano, B. Zibrowius, W. Schmidt, F. Schüth, *Microporous Mesoporous Mater.*, 2014, 200, 317.
- 7 W. Stöber, A. Fink, E. Bohn, Journal of Colloid and Interface Science, 1968, 26, 62.
- 8 X. Chen, J. Jiang, F. Yan, S. Tian, K. Li, RSC Adv., 2014, 4, 8703.
- B. Bharti, J. Meissner, U. Gasser, G. H. Findenegg, Soft Matter, 2012, 8, 6573.
- 10 D. Kumar, X. Wu, Q. Fu, J. W. Ho, P. D. Kanhere, L. Li, Z. Chen, Applied Surface Science, 2015, 344, 205.
- 11 F. Yan, J. Jiang, X. Chen, S. Tian, K. Li, *Ind. Eng. Chem. Res.*, 2014, **53**, 11884.
- 12 S. Kang, H. Y. Jeong, Journal of Hazardous Materials, 2015, 284, 143.
- 13 P. C. Ribeiro, R. Kiminami, A. Costa, Ceramics International, 2014, 40, 2035.
- 14 J. Ma, L. Li, J. Zou, Y. Kong, S. Komarneni, *Microporous Mesoporous Mater.*, 2014, 193, 154.
- 15 R. Ciriminna, A. Fidalgo, V. Pandarus, F. Béland, L. M. Ilharco, M. Pagliaro, *Chem. Rev.*, 2013, **113**, 6592.
- 16 A. M. Fidalgo, L. M. Ilharco, *Microporous Mesoporous Mater.*, 2012, **158**, 39.

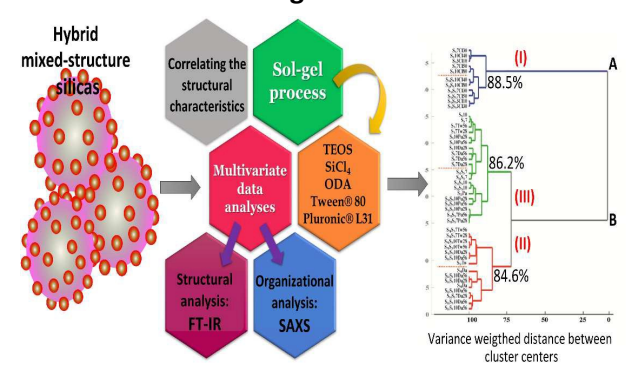
- 17 D. Stoeckel, D. Wallacher, G. A. Zickler, J. Perlich, U. Tallarek, B. M. Smarsly, *Phys. Chem. Chem. Phys.*, 2014, **16**, 6583.
- 18 Y. P. Moreno, M. B. Cardoso, E. A. Moncada, J. H. Z. dos Santos, *ChemPhysChem*, 2015, **16**, 2981.
- 19 J. F. A. de Oliveira, M. B. Cardoso, Langmuir, 2014, 30, 4879.
- 20 D. Mueller, M. F. Ferrão, L. Marder, A. B. da Costa, R. Schneider, *Sensors* 2013, **13**, 4258.
- 21 J. I. Robledo, H. J. Sánchez, L. L. Leani, C. A. Pérez, *Anal. Chem.*, 2015, **87**, 3639.
- 22 K. Banas, A. Banas, H. O. Moser, M. Bahou, W. Li, P. Yang, M. Cholewa, S. K. Lim, *Anal. Chem.*, 2010, **82**, 3038.
- 23 G. Veras, A. A. Gomes, A. C. da Silva, A. L. de Brito, P. B. de Almeida, E. P. de Medeiros, *Talanta*, 2010, **83**, 565.
- 24 A. B. Snyder, C. F. Sweeney, L. E. Rodriguez-Saona, M. M. Giusti, Food Chemistry, 2014, 147, 295.
- 25 S. Y. Song, Y. K. Lee, I. J. Kim, Food Chemistry, 2016, 190, 1027.
- 26 I. Jolliffe, Principal component analysis. Second Edition ed.; Springer-Verlag: New York, USA, 2002, 487.
- 27 M. Szymanska-Chargot, M. Chylinska, B. Kruk, A. Zdunek, *Carbohydrate Polymers*, 2015, **115**, 93.
- 28 G. Keppel, *Design and analysis: A researcher's handbook, 3rd ed.;* Prentice-Hall, Inc: Englewood Cliffs, 1991; pp 594.
- 29 S. Brunauer, P. H. Emmett, J. Am. Chem. Soc., 1938, 60, 309.
- 30 E. P. Barrett, L. G. Joyner, P. P. Halenda, *J. Am. Chem. Soc.*, 1951, **73**, 373.
- 31 A. Fidalgo, L. M. Ilharco, Chem. Eur. J., 2004, 10, 392.
- 32 G. Beaucage, J. Appl. Cryst., 1995, 28, 717.
- 33 G. Beaucage, H. K. Kammler, S. E. Pratsinis, J. Appl. Cryst., 2004, 37, 523.
- 34 H. K. Kammler, G. Beaucage, D. J. Kohls, N. Agashe, J. Ilavsky, J. Appl. Phys., 2005, 97, 054309.
- 35 J. Ilavsky, P. R. Jemian, J. Appl. Cryst., 2009, 42, 347.
- 36 D. Ballabio, Chemometrics and Intelligent Laboratory Systems 2015, **149**, Part B, 1.
- 37 Y. Jiang, H. Ge, F. Lian, Y. Zhang, S. Xia, RSC Advances 2015, 5, 93979.
- 38 A. Patras, N. Brunton, G. Downey, A. Rawson, K. Warriner, G. Gernigon, J. of Food Composition and Analysis 2011, 24, 250.
- 39 J. F. Hair, W. C. Black, B. J. Babin, in *Multivariate data analysis*. Upper Saddle River: Pearson Prentice Hall, 2006; pp 425-478.
- 40 37 T. J. Barton, L. M. Bull, W. G. Klemperer, D. A. Loy, B. McEnaney, M. Misono, P. A. Monson, G. Pez, G. W. Scherer, J. C. Vartuli, O. M. Yaghi, *Chem. Mater.*, 1999, 11, 2633.
- 41 H. Eltejaei, J. Towfighi, H. R. Bozorgzadeh, M. R. Omidkhah, A. Zamaniyan, *Materials Letters*, 2011, **65**, 2913.
- 42 A. Bernardes, C. Radtke, M. Alves, I. Baibich, M. Lucchese, J. H. Z. dos Santos, *J. Sol-Gel Sci. Technol.*, 2014, **69**, 72.
- 43 M. R. Yu, G. Suyambrakasam, R. J. Wu, M. Chavali, Sensors and Actuators B, 2012, 161, 938.
- 44 H. H. Chang, S. C. Chen, D. J. Lin, L. P. Cheng, *Journal of Membrane Science*, 2014, 466, 302.
- 45 Y. Liu, J. Gu, J. Zhang, F. Yu, J. Wang, N. Nie, W. Li, RSC Advances, 2015, 5, 9745.
- 46 T. Macher, J. Totenhagen, J. Sherwood, Y. Qin, D. Gurler, M. S. Bolding, Y. Bao, Advanced Functional Materials, 2015, 25, 490.

ARTICLE RSC Advances

- 47 C. J. Brinker, G. W. Scherer, Sol-gel science: the physics and chemistry of sol-gel processing, Academic Press: San Diego, 1990.
- 48 R. Tian, O. Seitz, M. Li, W. Hu, Y. J. Chabal, J. Gao, *Langmuir*, 2010, **26**, 4563.
- 49 A. Fidalgo, R. Ciriminna, L. M. Ilharco, M. Pagliaro, *Chem. Mater.*, 2005, **17**, 6686.
- 50 Y. P. Moreno, M. B. Cardoso, M. F. Ferrão, E. A. Moncada, J. H. Z. dos Santos, *Chemical Engineering Journal*, 2016, **292**, 233
- 51 P. A. Hartley, G. D. Parfitt, L. B. Pollack, *Powder Technology* 1985, **42**, 35.

- 52 G. D. Parfitt, Powder Technology, 1977, 17, 157.
- 53 C. J. Brinker, A. J. Hurd, K. J. Ward, J. D. Mackenzie, D. R. Ulrich, in *Ultrastructure processing of advanced ceramics*. Eds. JD Mackenzie and DR Ulrich, Wiley: New York, 1988; pp 223-270.
- 54 Y. Ma, X. Chen, X. Pi, D. Yang, J. Phys. Chem. C, 2011, **115**, 12822.
- 55 H. Park, G. Treich, Z. Helming, J. Morgan, C. Ryu, H. Hwang, G. Jung, *Macromol. Res.*, 2015, **23**, 13.
- 56 J. H. Z. dos Santos, P. P. Greco, F. C. Stedile, J. Dupont, Journal of Molecular Catalysis A: Chemical, 2000, 154, 103.

Table of contents image



New methodology to quickly identify changes in the structural properties of mesoporous silica materials through simultaneous multivariate analyses applied to techniques with different principles as SAXS curves and FT-IR spectra.